

# Multi-objective optimization determines when, which and how to fuse deep networks: an application to predict COVID-19 outcomes

Valerio Guarrasi<sup>a,b,\*</sup>, Paolo Soda<sup>a</sup>

<sup>a</sup>*Unit of Computer Systems and Bioinformatics, Department of Engineering, University Campus Bio-Medico of Rome, Italy*

<sup>b</sup>*Department of Computer, Control, and Management Engineering, Sapienza University of Rome, Italy*

---

## Abstract

The COVID-19 pandemic has caused millions of cases and deaths and the AI-related scientific community, after being involved with detecting COVID-19 signs in medical images, has been now directing the efforts towards the development of methods that can predict the progression of the disease. This task is multimodal by its very nature and, recently, baseline results achieved on the publicly available AIforCOVID dataset have shown that chest X-ray scans and clinical information are useful to identify patients at risk of severe outcomes. While deep learning has shown superior performance in several medical fields, in most of the cases it considers unimodal data only. In this respect, when, which and how to fuse the different modalities is an open challenge in multimodal deep learning. To cope with these three questions here we present a novel approach optimizing the setup of a multimodal end-to-end model. It exploits Pareto multi-objective optimization working with a performance metric and the diversity score of multiple candidate unimodal neural networks to be fused. We test our method on the AIforCOVID dataset, attaining state-of-the-art results, not only outperforming the baseline performance but also being robust to external validation. Moreover, exploiting XAI algorithms we figure out a hierarchy

---

\*Corresponding author

*Email address:* [valerio.guarrasi@uniroma1.com](mailto:valerio.guarrasi@uniroma1.com) (Valerio Guarrasi)

among the modalities and we extract the features' intra-modality importance, enriching the trust on the predictions made by the model.

*Keywords:* COVID-19, Deep-Learning, Multimodal Learning, Optimization

---

## 1. Introduction

It has been two years since the severe acute respiratory syndrome COVID-19 has struck the world with a pandemic causing millions of cases and deaths. Since the beginning, the scientific community has tried to contain the spread and the number of victims by studying the virus from multiple perspectives and looking for the best cures.

Among the various initiatives to combat the rising of the pandemic, researchers, practitioners and enterprises introduced new artificial intelligence (AI) methods and tools to process chest X-ray (CXR) and computed tomography (CT) examinations to replace or to supplement the reverse transcriptase-polymerase chain reaction (RT-PCR) tests. Both medical imaging procedures are instrumental in helping radiologists determine the source of symptoms, stratify the disease severity, and establish the best treatment plan for the patient's specific needs. On the other hand, CXR helps indicate abnormal formations of a large variety of chest diseases by using a very small amount of radiation. Reticular alteration (up to 5 days from the symptoms' onset) and ground-glass opacity (following 5 days from the symptoms' onset) are the CXR most frequent lesions in COVID-19 positive patients. The patients' consolidation gradually increases over time, striking mainly bilateral, peripheral, middle/lower locations. On the other hand, CT delivers a much higher level of detail, offering a computerized 360-degree view of the lungs' structures. However, by choosing this modality, we observed the lack of availability of machines' slots, the difficulty of moving bedridden patients, and long sanitation times. On the contrary, X-ray equipment is much smaller, less complex, and with lower costs than CT scans. For these reasons, in this work we focus on the use of CXR scans, that fit well with the COVID-19 crisis.

Most of the AI models for medical image-based applications, in particular those exploiting deep-learning (DL) models, consider only pixel-value data neglecting information available in other modalities. However, interpreting imaging findings is multimodal by its very nature and, hence, AI needs to be able to process together data coming from various modalities Baltrušaitis et al. (2018). Indeed, while multimodal learning is a well-established field of study Baltrušaitis et al. (2018); Ngiam et al. (2011), the potential of deep-learning shown processing unimodal data has recently motivated the rise of multimodal deep-learning (MDL), which aims to treat multimodal data by using deep network-based approaches. This should be very useful to progress in understanding the world around us, biomedicine included Ramachandram and Taylor (2017). In the specific context of the COVID-19 pandemic, MDL can support the patients' stratification by mining together images and clinical information Soda et al. (2021).

The literature agrees that the three main open questions in MDL are *when*, *which* and *how* the modalities must be joined to exploit their potential Stahlschmidt et al. (2022). Usually, MDL models are constructed by finding or combining the best model architecture for each modality, which are then combined by researchers and practitioners on the basis of the nature of the data, the task at hand and the networks' structure. However, this handcrafted approach does not necessarily provide the best ensemble Chen et al. (2020). To overcome these limitations, here we present a novel joint fusion technique that algorithmically finds the optimal set of deep architectures to be combined, whatever the modality they belong to, by maximizing both a classification evaluation metric and a measure of diversity among the learners. Indeed, diversity is an estimate of how the networks interpret data differently Kuncheva and Whitaker (2003). Next, the method trains the resulting architecture in an end-to-end fashion to carry out the task at hand. Further to determine which models and modalities should be fused, this work investigates when to join the different modalities and how to embed them in powerful multimodal data representations. We apply the method to stratify patients suffering from the COVID-19

syndrome by predicting the severity of the outcome using both clinical and CXR scans, showing that we achieve state-of-the-art results. Furthermore, to improve trust and transparency of our MDL approach, we present a novel combination of Explainable Artificial Intelligence (XAI) techniques not only illustrating the reasoning behind the decisions taken by the model, but also showing the relative contribution of each modality in making the decision.

The manuscript is organized as follows. Section 2 introduces the state-of-the-art of both multimodal fusion methods and DL applications of COVID-19 stratification. Section 3, illustrates the dataset on which the experiments were performed. Section 4 describes the novel fusion method presented in this work and the XAI algorithms used for interpretation. Section 5 introduces the experimental configuration in the context of COVID-19 prognosis prediction, whilst the corresponding results and explanations are offered in section 6. Finally, section 7 provides concluding remarks.

## 2. Background

With the spread of the epidemic, there has been a growth of interest in employing novel AI methods to fight the pandemic Chamola et al. (2020). The vast literature ranges from the use of traditional statistical models to the more complex DL networks. As it is out of the scope of this manuscript to mention the entire literature, here we give an overview of the state-of-the-art of DL applications predicting the disease’s outcome, focusing on those that used supervised MDL models and exploited a joint fusion between medical imaging and clinical data. Since the MDL method presented in this manuscript fits well with XAI algorithms, we also give an overview of this emerging field of study.

### 2.1. Multimodal Deep Learning

Multimodal data is composed of data originated by different sources observing a phenomena. The objective of MDL is to work with the data in a complementary manner to satisfy the undertaken learning task: instead of using manually designed or handcrafted modality-specific features, via DL we can

automatically learn and extract an embedded representation for each modality. Furthermore, here we focus on supervised multimodal fusion that joins information from different modalities for a classification or regression task. The literature agrees that understanding *when*, *which* and *how* modalities should be fused is the main challenge in MDL Baltrušaitis et al. (2018); Stahlschmidt et al. (2022).

To answer the first question (*when*), in the review Baltrušaitis et al. (2018) the authors divide multimodal fusion in model-agnostic and model-based methods. The former are feature-based or decision-based, being also named as early and late fusion, respectively. Early fusion consists in the integration of the raw multimodal data into a single feature vector which is used as input for the DL model. At its simplest form, early fusion consists in concatenating multimodal features, which can bring to a redundancy of information. Oppositely, late fusion consists in using multiple models trained on separate modalities, whose decisions are joint via an aggregation function or a meta-learner, aiming to augment the performance of each unimodal model Wu and Arribas (2003). Because model-agnostic fusions can suppress intra- or inter-modality interactions, in the last years researchers have mainly focused on model-based methods that allow intermediate fusion, also referred to as joint fusion, to occur directly inside the models. DL models transform raw inputs into higher-level representations through the alternation of linear and non-linear operations. With a MDL model, we obtain these representations for each modality which will be fused into a hidden layer creating a joint multimodal representation. Thanks to the fact that with DL we can have an end-to-end training of all the multimodal representation components and the fusion component, the training phase essentially consists in learning hierarchical representations from raw data, which give rise to an optimized intermediate-level fusion representation Bengio et al. (2013). This is why we can consider joint fusion an evolution of early fusion. Furthermore, inside a joint model, to understand when the unimodal architectures should be joined and to find the fusion structure, the majority of the available work follows a meticulous handcrafted approach. For instance, in Neverova et al.

(2015); Karpathy et al. (2014) the authors adopted a single fusion layer from which they implement a gradual fusion strategy to automatically comprehend when to fuse the modalities.

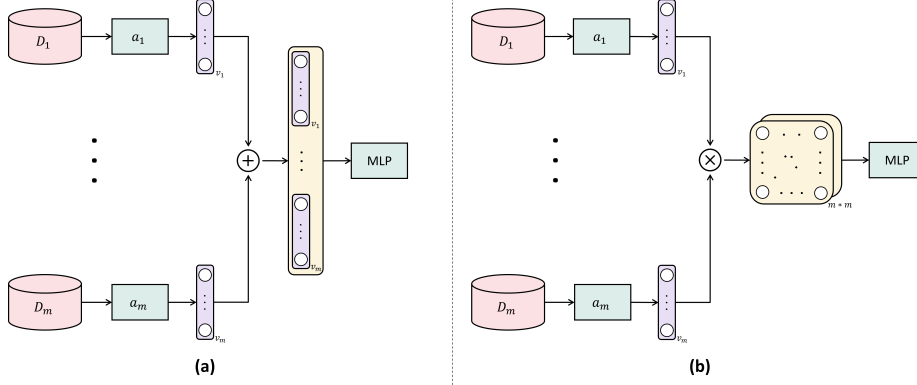
Let us now focus on the second challenge, which aims to understand *which* modalities should be fused and with which models. With the increasing number of high-performing deep architectures, the selection of the one best suited for each modality is a hard process. The choice of which modality to fuse is usually based on intuition and on a trial and error approach that, usually, first fuses similar modalities and then tries to integrate disparate modalities Baltrušaitis et al. (2018). Furthermore, prior investigations on the data, as well as feature selection techniques, should allow us to find redundant information along the modalities Kumar and Minz (2014). Shifting the attention to the choice of which neural networks should be fused, the analysis of the literature shows that the deep architectures are usually chosen by analyzing the single modalities Soda et al. (2021); Chen et al. (2020), and no optimal multimodal architecture selection is overtaken.

Focusing on the third question, in the literature there are various techniques studying *how* to obtain an embedded representation that helps the unimodal models in the desired tasks. In joint fusion, the state-of-the-art adopts two main methodologies Nojavanasghari et al. (2016); Zadeh et al. (2017). The first is a simple but effective way that concatenates the extracted vectors from a given layer of each unimodal model Nojavanasghari et al. (2016). The next hidden layer combines the different modalities by computing

$$f\left(\sum_{i=1}^m w_i^T v_i\right) \quad (1)$$

where  $v_i$  and  $w_i$  are the encoding and the weights of the model of the  $i^{th}$  modality,  $f$  is the activation function and  $m$  stands for the number of modalities involved. The second approach consists of a multiplicative method computing the outer product  $\otimes$  (or Kronecker product) of all the  $m$  modality-specific feature vectors, extrapolated from a given hidden layer, exploiting the intra- and

Figure 1: Multimodal joint-fusion methods: a) concatenation method Nojavanasghari et al. (2016) b) multiplicative method Zadeh et al. (2017).



inter-modality relations Zadeh et al. (2017). The layer output is:

$$\bigotimes_{i=1}^m \begin{bmatrix} v_i \\ 1 \end{bmatrix} \quad (2)$$

where the 1 is appended to the encoding  $v_i$  so that all unimodal and multimodal combinations interactions are represented. A schematic visualization of both joint fusion methods is shown in figure 1.

Many studies such as Ramachandram et al. (2018); Kim and Frahm (2018); Joze et al. (2020) dealt with determining an automatic methodology on how and when to fuse modalities, but none have focused on finding an optimized way for choosing which model architectures for each modality should be fused. Therefore, we hereby propose a strategy to find the best combination of models of the different modalities.

## 2.2. DL and COVID-19

The application of AI to the COVID-19 data analysis has been directed towards medical imaging and clinical data addressing two main issues: *i*) the detection of patients suffering from COVID-19 pneumonia from those which are

healthy or affected by different types of pneumonia and, *ii*) the prediction of the outcome.

In the former case, a large number of publications have been produced, as reviewed in Wynants et al. (2020). Many of them leverage the open-source CXR COVID-19 data collection Cohen et al. (2020), or specific clinical datasets. Moreover, there are also papers that use CT scans, as reviewed in Ozsahin et al. (2020), or that use other imaging modalities Wynants et al. (2020). Instead, in the prediction scenario, few works have investigated the stratification of the disease to distinguish between patients with mild and severe outcomes Soda et al. (2021); Signoroni et al. (2021); Zhu et al. (2020); Al-Najjar and Al-Rousan (2020); Bai et al. (2020); Ning et al. (2020); Fang et al. (2021). In this respect, the rest of this subsection overviews such papers since outcome prediction is the focus of our work.

Considering the publications which work with CXR scans only, in Signoroni et al. (2021) the authors designed an end-to-end convolutional neural network (CNN) architecture for predicting a multi-regional score conveying the degree of lung compromised in COVID-19 patients.

Focusing on the publications using clinical data only, in Zhu et al. (2020) the authors presented a DL algorithm, whose architecture is composed of 6 fully connected (FC) dense layers with ReLU as activation function, which identifies the top clinical variable predictors and derived a risk stratification score system to help clinicians triage COVID-19 patients. Their model was trained on a private dataset with 181 patients and of 56 clinical variables, obtaining an AUC equal to 0.968. Similarly, in Al-Najjar and Al-Rousan (2020) the authors built a neural network with one hidden layer to predict the status of recovered and death COVID-19 patients in South Korea. They used seven different clinical variables and obtained an accuracy equal to 0.966 on a private dataset composed of 1308 patients.

As interpreting medical data is a multimodal process by its very nature, we now present the four works that use both clinical data and medical images, also noticing that three of them use CT images Bai et al. (2020); Ning et al. (2020);



Fang et al. (2021) and only one made use of CXR scans Soda et al. (2021). In Bai et al. (2020) the authors introduced a DL-based method using 53 clinical features and quantitative CT data to detect mild patients with a potential malignant progression. The authors use a multi-layer perceptron (MLP) on the clinical features creating an embedding that is concatenated with the flattened CT, which are then fed to a Long short-term memory (LSTM) network and a FC network, achieving an accuracy of 0.792 on a cohort of 199 patients belonging to a private dataset. Next, in Ning et al. (2020) the authors use both CT images and 130 clinical features to discriminate between negative, mild and severe COVID-19 cases via a DL framework based on the VGG-16 and a 7-layer FC network. This network was trained on a public dataset containing 1521 patients, and it obtained an accuracy equal to 0.811. Furthermore, the authors of Fang et al. (2021) developed an early-warning system with DL techniques to predict COVID-19 malignant progression leveraging CT scans and the clinical data of the patients. The authors use a 3D ResNet and MLP to encode the chest CT scans and the 61 clinical features, respectively, whose features are concatenated and fed into an LSTM and several FC networks to make the prediction, obtaining an accuracy equal to 0.877, on a private dataset with 1040 patients.

Let us now turn the attention to the only work that, to the best of our knowledge, uses CXR images and clinical for the COVID-19 prognosis Soda et al. (2021). In this paper, the authors not only made publicly available a dataset designed for the mild and severe stratification task, but they also presented three different multimodal AI approaches that can be used as a baseline performance for future improvement. In the first learning approach, also referred to as handcrafted approach (HC), the authors employed first order and texture features computed from the images, which are mined together with the clinical data feeding a supervised learner, such as Support Vector Machines and Random Forests. The second approach is named hybrid (HYB) and it mixes automatically extracted features computed by a pre-trained CNN with the clinical data, which are then fed to a classifier as before. The last approach is an

end-to-end approach (ETE) exploiting together the clinical data and the raw CXR by using a multi-input CNN. The best results are obtained by the ETE approach, whose results are reported and discussed in section 6.

This analysis of the literature shows that the development of AI-based models predicting the outcomes of COVID-19 patients still deserves further research efforts, since in the multimodal scenario only simple methods are employed with no interest in understanding *when*, *which* and *how* the neural networks architectures should be used to find the appropriate fusion. We decided to use Soda et al. (2021) as our starting point, given the importance of their multimodal data, and we will show that our proposed MDL framework improves the performance available at the state-of-the-art.

### 2.3. XAI

The major disadvantage of neural network approaches is their lack of interpretability Arrieta et al. (2020). It is hard to understand what the predictions rely on, and which modalities and features hold an important role Joshi et al. (2021). For this reason the number of XAI algorithms has grown in the last few years. In general, an XAI algorithm is one that produces information to make a model’s functioning clear or easy to understand. The literature makes a clear distinction among models that are interpretable by design (transparent models), and those that can be explained by means of external XAI techniques (post-hoc explainability). Given the complex structure of DL algorithms, post-hoc model-specific XAI models have been developed Montavon et al. (2017); Shrikumar et al. (2017); Hendricks et al. (2018); Selvaraju et al. (2017); Sundararajan et al. (2017). Focusing our attention to tabular or image data, i.e. the one used in this work, in the literature we found algorithms presenting feature relevance explanations specific for these modalities taken alone. For example, according to Arrieta et al. (2020), Deep Taylor decomposition Montavon et al. (2017) and DeepLIFT Shrikumar et al. (2017) are the most used XAI models specific for multi-layer neural networks which work on tabular data, Equalizer Hendricks et al. (2018) and Grad-CAM Selvaraju et al. (2017) are suited

for CNNs working on image data, whereas Integrated Gradients should be used by both network typologies Sundararajan et al. (2017).

The literature is well advanced in models which work on a single modality Arrieta et al. (2020) but it lacks research for MDL. In this respect, the multimodal method that we present brings along the possibility to apply and combine any unimodal XAI algorithms in a way to understand the contribution that each modality and each data within a modality has during the prediction.

### 3. Materials

We performed the experiments on the AIforCOVID imaging archive Soda et al. (2021) since it is the only publicly available multimodal dataset on COVID-19 stratification at the time this research was carried out. It includes 820 CXR scans and clinical data collected from six different hospitals at the time of hospitalization of symptomatic patients positive to the SARS-CoV-2 infection at the TR-PCR test. The 34 clinical available parameters are listed in Table A.1, and for further details the interested readers can refer to Soda et al. (2021).

On the basis of the clinical outcome, each patient was assigned to the mild or severe group, where the mild group consists of the patients that were sent back to domiciliary isolation or were hospitalized without any ventilatory support, whilst the severe group is composed of patients who required non-invasive ventilation support, intensive care unit or patients who deceased.

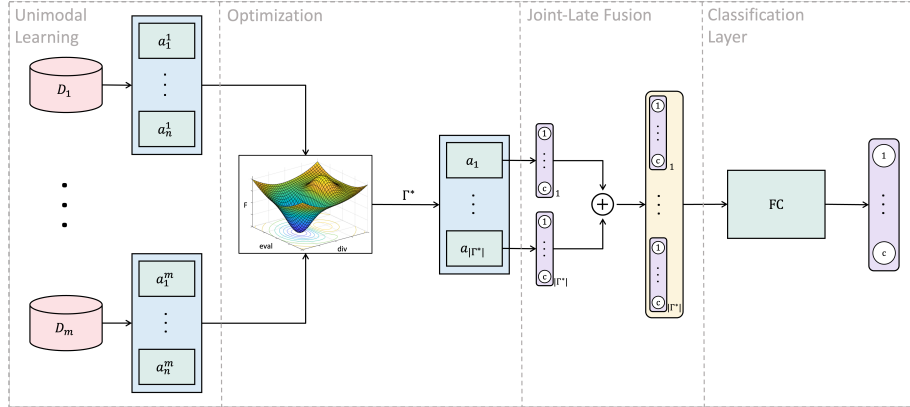
Recently, a second release of the dataset was made available and it is composed of other 283 patients, whose data were collected in other two new centers. Here, we use these data as an external validation set in a way to have further proof that the proposed framework is robust on never seen data.

### 4. Methods

#### 4.1. Multimodal Learning

To predict the severity outcome of COVID-19 patients exploiting both the pixel information of their CXR scan and their clinical information, we propose

Figure 2: Multimodal joint-late method: for each  $m$  modalities,  $n$  models are trained to find the optimal combination  $\Gamma^*$ , whose classification vector is passed to a FC neural network which will output the desired classification out of the  $c$  classes.



a novel supervised end-to-end joint fusion method, which maximizes the advantages brought by all the given modalities. It first looks for the best combination of models, which are then joint and trained to carry out the given classification task. This is visually summarized in Figure 2, which is organized in four main blocks that are now detailed, one per paragraph.

*Unimodal Learning.* The proposed method can be applied to an arbitrary number of  $m$  different modalities and  $n$  different neural network architectures.

Let us first introduce the application matrix  $\Theta \in \text{Mat}_{m \times n}$ , where each element is defined as follows

$$(\Theta)_{ij} = \theta_{ij} = \begin{cases} 1 & \text{if the } j^{\text{th}} \text{ model processes data of the } i^{\text{th}} \text{ modality} \\ 0 & \text{if the } j^{\text{th}} \text{ model does not process data of the } i^{\text{th}} \text{ modality} \end{cases} \quad (3)$$

Hence,  $\theta_{ij}$  represents the use of the  $j^{\text{th}}$  model for the  $i^{\text{th}}$  modality, with  $i \in \{1, \dots, m\}$  and  $j \in \{1, \dots, n\}$ . Furthermore, let us denote with  $a_j$  any neural network architecture we would like to use; on this basis, when  $\theta_{ij} = 1$ ,  $a_j^i$  denotes that the architecture  $a_j$  is trained on data from the  $i^{\text{th}}$  modality. The set of

networks that will be combined is denoted by

$$\Gamma_I = \{a_j^i | \theta_{ij} = 1, \forall (i, j) \in I\} \quad (4)$$

where  $I$  contains a subset of all possible pairs of models and modalities:

$$I \subseteq \{1, \dots, m\} \times \{1, \dots, n\} \quad (5)$$

Consequently, the number of different configurations for  $\Gamma_I$  is equal to  $\sum_{h=2}^s \binom{s}{h}$ , where  $s = \sum_{i=1}^m \sum_{j=1}^n \theta_{ij}$ . Furthermore, model architectures being part of  $\Gamma_I$  depend on the corresponding  $\Theta$  matrix, whilst the choice of the number of models  $n$  and which models to include should consider the constraints of the application, such as any limit in computational resources.

It is worth noting that the framework now introduced goes beyond the state-of-the-art of multimodal joint networks, which usually use only one model for each modality Chen et al. (2020). On the contrary, we consider the chance of having several models per modality, a situation that researchers and practitioners often meet in practice. In these cases, usually they first heuristically determine the best model per modality in a pool of many, i.e.  $\Gamma_I$ , and they combine such “best” models in a multimodal learner Arrieta et al. (2020). However, this approach neglects any possible interaction between models and modalities, so that the combination of best unimodal models does not necessarily reflect the best multimodal architecture. Furthermore, the general assumption that a multimodal model should be composed of a single model per modality is also a too much straightforward simplification.

*Optimization.* To go beyond the naive use of  $\Gamma_I$ , we deem that it should be more useful to work with all the modalities and all the models together. The first step is to detect which is the subset of models to be combined to get the best multimodal architecture providing the best multimodal data representation. This subset is determined by solving a multi-objective maximization problem that leverages on two scores computed on a validation set for each  $\Gamma_I$  Guarrasi et al. (2022, 2021). The first score is any measure derived from the confusion matrix, shortly referred as  $\text{eval}(\Gamma_I)$ , whilst the second is a measure of the diversity

between the unimodal learning models, denoted as  $\text{div}(\Gamma_I)$ . To find optimal combination of models from  $\Gamma_I$  exploiting at best all the modalities, denoted by  $\Gamma^*$ , the algorithm works as follows. Using a cross-validation approach, we first apply each model  $a_j^i$ , that was trained on the corresponding unimodal dataset  $D_i$ , to a validation set. Then, we compute the average of both  $\text{eval}(\Gamma_I)$  and  $\text{div}(\Gamma_I)$  among the cross-validation runs for all the possible  $\Gamma_I$ s, finally finding the combination  $\Gamma^*$  which maximizes both metrics. This means that we look for the  $\Gamma_I$  that, on the one side, returns the best classification performance and, on the other side, reduces the incidence and effect of coincident errors among its members, thus considering possible relationships between models and modalities.

It is worth noting that such a process corresponds to solving a multi-objective optimization problem. In fact, given the pair  $P = (F, C)$ , where  $F = \{f_1(x), \dots, f_a(x)\}$  is the set of  $a$  objective functions that we want to maximize and  $C = \{c_1(x) \leq 0, \dots, c_b(x) \leq 0\}$  are the  $b$  constraints, where if  $x \in C$  it is said to be an admissible point for  $P$ . Given two admissible points  $x_1$  and  $x_2$  for  $P$ ,  $x_1 \succ x_2$  means that  $x_1$  dominates  $x_2$ . This means that  $f_\alpha(x_1) \leq f_\alpha(x_2) \forall \alpha \in \{1, \dots, a\}$ , and  $f_\alpha(x_1) < f_\alpha(x_2)$  for at least one  $\alpha \in \{1, \dots, a\}$ . A Pareto optimum  $x^*$  is an admissible point for  $P$  if  $x^* \succ x$  for any other admissible points  $x$  for  $P$ . i.e. it tries to minimize all functions in  $F$  under the constraints  $C$ , solving a multi-objective minimization problem over  $P$ . Based on John (2014), the point  $x^*$  is a Pareto optimum if there exist  $\lambda$  and  $\mu$  satisfying the following system:

$$\left\{ \begin{array}{l} \sum_{\alpha=1}^a \lambda_\alpha \nabla f_\alpha(x^*) + \sum_{\beta=1}^b \mu_\beta \nabla c_\beta(x^*) = 0 \\ \sum_{\beta=1}^b \mu_\beta c_\beta(x^*) = 0 \\ \lambda_\alpha \geq 0 \quad \forall \alpha = 1, \dots, a \\ \mu_\beta \geq 0 \quad \forall \beta = 1, \dots, b \\ (\boldsymbol{\lambda}, \boldsymbol{\mu}) \neq (0, 0) \end{array} \right. \quad (6)$$

In our framework,  $\Gamma^*$  is the Pareto Optimum maximizing both two scores, related to the confusion matrix and to the diversity, respectively. This implies

that  $\text{eval}(\Gamma_I)$  and  $\text{div}(\Gamma_I)$  are the two objective functions ( $a = 2$ ). Thus,  $\Gamma^*$  is a Pareto optimum if the quintuple  $(\lambda_1^*, \lambda_2^*, \mu_1^*, \mu_2^*, \Gamma^*)$  satisfies the following system:

$$\begin{cases} \lambda_1(-\dot{\text{eval}}(\Gamma_I)) + \lambda_2(-\dot{\text{div}}(\Gamma_I)) + \mu_1 - \mu_2 = 0 \\ \lambda_1 \geq 0, \lambda_2 \geq 0, \mu_1 \geq 0, \mu_2 \geq 0 \end{cases} \quad (7)$$

where  $\dot{\text{eval}}(\Gamma_I)$  and  $\dot{\text{div}}(\Gamma_I)$  denotes the first derivative of such quantities. Observing that both  $\text{eval}(\Gamma_I)$  and  $\text{div}(\Gamma_I)$  range in  $[0, 1]$ , and under the hypothesis that  $\text{eval}(\Gamma_I) = 1$  in case of perfect outcome prediction <sup>1</sup> we can write the following minimization function:

$$(\text{eval}(\Gamma_I) - 1)^2 + (\text{div}(\Gamma_I) - 1)^2 \quad (8)$$

Following Kuhn and Tucker (2014), we can solve this system:

$$\begin{cases} 2(\text{eval}(\Gamma_I) - 1)\dot{\text{eval}}(\Gamma_I) + 2(\text{div}(\Gamma_I) - 1)\dot{\text{div}}(\Gamma_I) + \mu_1 + \mu_2 = 0 \\ \mu_1 \geq 0, \mu_2 \geq 0 \end{cases} \quad (9)$$

Going forward this can be rewritten as:

$$\begin{cases} 2(1 - \text{eval}(\Gamma_I))(-\dot{\text{eval}}(\Gamma_I)) + 2(1 - \text{div}(\Gamma_I))(-\dot{\text{div}}(\Gamma_I)) + \mu_1 + \mu_2 = 0 \\ \mu_1 \geq 0, \mu_2 \geq 0 \end{cases} \quad (10)$$

$(\lambda_1^*, \lambda_2^*, \mu_1^*, \mu_2^*, \Gamma^*)$  satisfies the system and  $\Gamma^*$  is a Pareto optimum for our optimization problem, when  $\lambda_1^* = 2(1 - \text{eval}(\Gamma_I))$  and  $\lambda_2^* = 2(1 - \text{div}(\Gamma_I))$ , where  $\lambda_1^* \geq 0$  and  $\lambda_2^* \geq 0$  since  $0 \leq \text{eval}(\Gamma_I) \leq 1$  and  $0 \leq \text{div}(\Gamma_I) \leq 1$ .

Moreover, with this optimization approach, if a modality is useless for the given classification task, all the networks working on that modality will be discarded.

*Joint-Late Fusion.* So far we presented an approach to find the optimal multimodal combination model, i.e. *which* modalities and related models should be

---

<sup>1</sup>Straightforwardly, if  $\text{eval}(\Gamma_I)$  is an error-related measure, i.e.  $\text{eval}(\Gamma_I) = 0$  in case of perfect outcome prediction, equation 8 can be rewritten as  $\text{eval}(\Gamma_I)^2 + (\text{div}(\Gamma_I) - 1)^2$ .

included into the multimodal architecture, but we have not defined *how* and *when* to actually join the models  $a_j^i$  in  $\Gamma_I$ . To simplify the notation, we now omit the apex  $i$ , denoting the learners included in  $\Gamma_I$  as  $a_j$ , with  $j = 1, \dots, |\Gamma_I|$ . Each of these models provides a classification vector  $\mathbf{y}_j = [y_{j1}, \dots, y_{jp}, \dots, y_{jc}]^T$ , where  $c$  is the number of classes and  $p$  is the generic  $p^{\text{th}}$  output neuron. Each entry  $y_{jp}$  is defined using the parameterized softmax function:

$$y_{jp} = \text{softmax}_k(z_p^{(j)}) = \frac{e^{kz_p^{(j)}}}{\sum_{t=1}^c e^{kz_t^{(j)}}} \quad (11)$$

where  $k > 0$ , and  $z_p^{(j)}$  denotes the  $p^{\text{th}}$  value of the output layer neuron internal activity for the network  $a_j$ ; similar definition holds for  $z_t^{(j)}$ . Note that for  $k = 1$  each element represents an estimate of the classification posterior probability for each class of each model.

On these premises, to join the models we define a *soft* shared representation given by  $[\mathbf{y}_1^T, \dots, \mathbf{y}_{|\Gamma_I|}^T]^T$ , which corresponds to concatenate the classification vectors, an approach similar to concatenating the hidden layers as in Nojavanasghari et al. (2016). Hence, this shared representation vector is composed of  $c \cdot |\Gamma_I|$  elements. Furthermore, if  $k \rightarrow \infty$ ,  $\mathbf{y}_j$  becomes a binary vector with only one element equal to one, allowing us to get a *crisp* shared representation containing the binary outputs, which provides a direct interpretation of the embedded layer.

*Classification Layer.* This shared representation, being either soft or crisp, is then passed to a FC neural network, with  $c$  neurons in the last layer, that performs the intermediate fusion. Note that here we exploit the advantages of both joint and late fusion, since the classifications of the sub-networks are aggregated via an end-to-end manner using the back-propagation during the training process that minimizes the overall loss function. Indeed, it avoids the combination of features belonging to different spaces, while it combines the deep neural networks into a common classification space, and it is shortly referred to as to *joint-late* fusion in the following.



#### 4.2. XAI

The nature of the joint-late fusion approach, makes interpretability simple and effective. First, the weights  $w$  coming out of the embedded classification vector connected to the first layer of the FC network, provides useful information because it reveals the importance of each class for each model and, consequently, the importance of each modality. The higher the value of  $w_i$  with  $i = 1, \dots, n$ , the higher is the contribution for the combined classification coming from  $i^{th}$  model. Furthermore, as more models per modality are allowed, we can also understand the models that contribute more in the final classification for each class by looking at the weights proportion within each modality.

It is worth noting that any XAI algorithm, being model-agnostic or model-specific, can be applied to our MDL architecture, because it is composed of multiple models which can be interpreted one by one. For instance, if one of the modalities uses tabular data and the chosen models are FC neural networks, any post-hoc model-specific XAI algorithm for multi-layer neural networks can be applied on the single models to understand the importance of each tabular variable Montavon et al. (2017); Shrikumar et al. (2017). Moreover, if another modality consists of images and the models used are CNNs, we can use a post-hoc model-specific XAI algorithm to deduce the contribution of each image’s pixel to the classification Hendricks et al. (2018); Selvaraju et al. (2017). Going forward, there are also XAI algorithms that work on models regardless of the used modalities, that when applied to CNNs or FC networks, we understand the contributions for the classification of each image pixel and of each tabular variable, respectively Sundararajan et al. (2017). Since the model we propose is composed of multiple neural networks (both FC and CNNs as presented in section 5), we can apply all the before-mentioned XAI algorithms on the corresponding network and sub-networks.

Given the fact in our framework we can have multiple models working with the same modality, we now introduce the concept of weighted XAI: it combines the outputs of the XAI algorithms specific to a modality with the weights coming from the embedded classification vector. Since these weights make us

understand the contribution of each model, we combine the different XAI importances via a weighted sum to obtain a single interpretation of the modality. Hence for each feature  $e_w$  the output of the weighted XAI algorithm importance is:

$$\mathbf{e}_w = \mathbf{e} \cdot \mathbf{w} \quad (12)$$

where each contribution  $\mathbf{e}_i$  extracted from the  $n$  unimodal models is weighted with the corresponding layer weight  $\mathbf{w}_i$  and summed together. For example, if we are working on the image modality and we apply Grad-CAM Selvaraju et al. (2017) to all the corresponding CNNs, we obtain a feature map for each model. By computing the dot product between the maps and the weight vector, we get a single feature map explaining which pixels contributed more or less to that specific classification. The same considerations hold for tabular data.

## 5. Experimental Configuration

In this section we introduce the different experiments we performed. Furthermore, to avoid any bias when comparing the baseline results of Soda et al. (2021) that released the AIforCOVID dataset with the ones achieved by the learning framework presented here, we applied the same pre-processing procedure and validation approach, shortly described in subsections 5.1 and 5.5, respectively.

### 5.1. Data Pre-processing

We use the 34 clinical descriptors available with the AIforCOVID repository, which are not direct indicators of the prognosis, that are listed in the appendix Table A.1. Missing data were imputed using the mean and the mode for continuous and categorical variables, respectively. Finally, to have the features all in the same range, a min-max scaler was applied along the variables.

In the case of CXR scans we extracted the segmentation mask of lungs, using a pre-trained U-Net Ronneberger et al. (2015) on two non-COVID-19 datasets Shiraishi et al. (2000); Jaeger et al. (2014). The mask was used to

extrapolate the minimum squared bounding box containing both lungs, which is then resized to 224x224 and normalized with a min-max scaler bringing the pixel values between 0 and 1. As already mentioned, the interested readers can refer to Soda et al. (2021) for further details.

## 5.2. Classification

As introduced in section 4, the first step to follow to obtain the optimal  $\Gamma^*$  network is to train and evaluate different models using the data of the two modalities, i.e. CXR scans and clinical data.

For the image modality we worked with 30 different CNNs that come from 8 different main architectures:

- AlexNet Krizhevsky (2014);
- VGG Simonyan and Zisserman (2014): VGG11, VGG11-BN, VGG13, VGG13-BN, VGG16, VGG16-BN, VGG19, VGG19-BN;
- ResNet He et al. (2016): ResNet18, ResNet34, ResNet50, ResNet101, ResNet152, ResNeXt50, ResNeXt101, Wide-ResNet50-2, Wide-ResNet101-2;
- DenseNet Huang et al. (2017): DenseNet121, DenseNet169, DenseNet161, DenseNet201;
- GoogLeNet Szegedy et al. (2015);
- ShuffleNet Ma et al. (2018): ShuffleNet-v2-x0-5, ShuffleNet-v2-x1-0, ShuffleNet-v2-x1-5, ShuffleNet-v2-x2-0;
- MobileNetV2 Sandler et al. (2018);
- MNasNet Tan et al. (2019): MNasNet0-5, MNasNet1-0;

In all the cases the weights were initialized using the values pre-trained on the ImageNet dataset Deng et al. (2009); we also changed the output layer dimension to 2 neurons, one for each class.

In the case of clinical information, which are tabular data, we adopted 4 MLPs that differ in terms of depth and wideness of the model. We opted to use such architectures since these feedforward networks are able to learn a low-dimensional representation before being fused with the other modality Glorot and Bengio (2010). In particular, the models’ hidden layers have the following organizations:

- MLP-1: it has 3 hidden layers with 64, 64, 32 neurons respectively;
- MLP-2: it has 5 hidden layers with 64, 128, 128, 64, 32 neurons respectively;
- MLP-3: it has 7 hidden layers with 64, 128, 256, 256, 128, 64, 32 neurons respectively;
- MLP-4: it has 9 hidden layers with 64, 128, 256, 512, 512, 256, 128, 64, 32 neurons respectively;

A ReLU activation function is applied on all layers, since it learns several times faster than regular sigmoid activation functions Glorot et al. (2011), despite its non-differentiability at zero. Straightforwardly, the input layer and the output layers consist of 34 and 2 neurons, respectively.

Turning our attention to the matrix  $\Theta$ , it is composed of 24 columns ( $n = 24$  the number of architectures) and two rows ( $m = 2$  the number of modalities).

Furthermore, as for the two objective functions  $\text{eval}(\Gamma_I)$  and  $\text{div}(\Gamma_I)$  we adopt the accuracy (Acc) and the correlation coefficient ( $\rho$ ), respectively. Note that the accuracy is computed on the models part of the  $\Gamma_I$ s in late-fusion via the majority voting aggregation function. We opted for late fusion optimization to prevent the training of all the  $\sum_{h=2}^s \binom{s}{h}$  end-to-end ensemble models. In this way, we only train  $n$  single models, apply the optimization, and conclude with one final embedded training of  $\Gamma^*$ .

Majority voting consist in finding the most common classification  $c$  between all the classifications  $c_i$  extracted by the  $|\Gamma_I|$  unimodal trained models

$$c = Mo(c_i | 1 \leq i \leq |\Gamma_I|) \tag{13}$$

where  $Mo$  indicates the mode of a set and  $|\Gamma_I|$  is the number of models in  $\Gamma_I$ . The correlation coefficient  $\rho$  instead between two classifiers is defined as:

$$\rho_{ij} = \frac{n^{11}n^{00} - n^{01}n^{10}}{\sqrt{(n^{11} + n^{10})(n^{01} + n^{00})(n^{11} + n^{01})(n^{10} + n^{00})}} \quad (14)$$

where  $n^{00}$  is the number of wrong classifications made by both models,  $n^{11}$  is the number of correct classifications made by the models,  $n^{10}$  and  $n^{01}$  are the number of instances on which the classifications of the two models differ. Since  $\rho$  is a pairwise measure, the overall diversity in  $\Gamma_I$  is given by:

$$\rho(\Gamma_I) = \frac{2}{|\Gamma_I|(|\Gamma_I| - 1)} \sum_{i=1}^{|\Gamma_I|-1} \sum_{j=i+1}^{|\Gamma_I|} \rho_{ij} \quad (15)$$

Going beyond the single models, after determining  $\Gamma^*$ , its models are joint via the joint-late fusion method introduced in 4.1. As mentioned there, the classification space can be built adopting a soft and a crisp shared representation. This permits us to investigate two learners, denoted as JLF-S and JLF-C, respectively. We also investigate what happens by varying the final FC layer, lying after the shared representation. To this end, we tested two different FC layers: the first does not have any hidden layers but directly connects the joint vector to the output classification layer using a single perceptron, and it is denoted using the ending 1. The second consists of a single hidden layer of 4 neurons connected to the output classification layer, which is denoted using the ending 2. The former permits us to investigate linear combinations among the classifications of the networks, whilst the latter investigates non-linear combinations. In summary, we investigate four set-ups for the joint-late approach we present, i.e. JLF-S-1, JLF-S-2, JLF-C-1 and JLF-C-2.

### 5.3. Training Configuration

For both the single model and the multimodal scenarios, we adopt the training procedure described in Soda et al. (2021); so that any variation in performance is given only by the enhancements brought by the method and not by any other reason. To prevent overfitting of the CNNs, we randomly applied the

following image transformations with a probability equal to 0.3: horizontal or vertical shift ( $-20 \leq \text{pixels} \leq 20$ ), random zoom ( $0.9 \leq \text{factor} \leq 1.1$ ), vertical flip, random rotation ( $-15^\circ \leq \text{angle} \leq 15^\circ$ ), and elastic transform ( $20 \leq \alpha \leq 40$ ,  $\sigma = 7$ ). Both the CNNs and the MLPs were trained using the cross-entropy loss, regulated by an Adam optimizer with an initial learning rate of 0.001, which is scheduled to reduce by an order of magnitude every time the minimum validation loss doesn't change for 10 consecutive epochs. To prevent overtraining and overfitting we fix the number of maximum epochs to 300, with an early stopping of 25 epochs on the validation loss. We do not perform any preliminary optimization of the networks hyperparameters because in Arcuri and Fraser (2013) the authors empirically reported that fine-tuning the learner parameters provides performance that do not statistically differ from those attained using the default values, a claim also confirmed by the experiments presented in Soda et al. (2021) on the AIforCOVID dataset. Furthermore, we do not pre-train the networks on another CXR dataset: indeed, although this would help the models learn modality-specific feature representations Rajaraman et al. (2020), the results available on the AIforCOVID dataset show that this practice does not introduce any significant performance improvement Soda et al. (2021).

All the experiments were trained by using a batch size of 32 on a NVIDIA TESLA V100 GPU with 16 GB of memory, using PyTorch as the main DL coding library.

#### 5.4. Competitors

To verify that the end-to-end process actually brings a performance enhancement, and to check that the joint network is not actually learning a late-fusion via FC layers using as input the classifications of the different networks, we froze the joint networks up to the joint classification vector and trained only the last FC classifier, creating a late fusion method. We would expect that if there is an actual benefit in the joint end-to-end to fusion, these performances would be lower. We will denote these experiments with: LF-S-1, LF-S-2, LF-C-1 and LF-C-2, where the S and the C encodings refer to the soft and the crisp

embedded classification vectors and 1 and 2 refer to the type of FC layers employed, as before. Finally, note that for all the experiments where joint training was performed (i.e. JLF-C-1, JLF-C-2, JLF-S-1, JLF-S-2, JF-C, JF-M), the weight initialization is performed by using the weights of the networks trained singularly.

We also compare the results of the joint-late fusion with those attained by the majority voting late fusion approach applied to the models included in  $\Gamma^*$ , denoted as LF-MV. Since majority voting is the aggregation function used in the optimization phase, this comparison permits us to not only investigate if the joint-late training is beneficial, but also to compare our proposal against a late-fusion technique, addressing the question on *when* the models should be fused. We also tested the concatenation (denoted as JF-C) and the multiplication methods (denoted as JF-M) introduced in section 2.1: the comparison of these approaches against the JLF solutions lets us deepen *how* the single models should be aggregated. For the sake of completeness, we would note that the JLF approach intrinsically studies *which* learners should be fused and, in the next section 6 we also compare the results against the use of a single network.

Finally, as natural competitors, we also compare our results with those presented in the work introducing the AIforCOVID dataset Soda et al. (2021), i.e. the HC, HYB and ETE methods summarized in section 2.

### 5.5. Validation Approach

The experiments were ran in 10-fold stratified cross-validation (CV), and leave-one-center-out cross-validation (LOCO), following the same experimental procedure described in Soda et al. (2021), thus ensuring a fair competitor between the approaches. In each CV fold the proportion between the training, validation and testing sets is 70%-20%-10%, respectively.

In LOCO validation we study how the models generalize to different data sources: indeed, in each fold the test set contains all the samples belonging to one center only, while the instances of the other six centers were assigned to the training and validation set.

With reference to Soda et al. (2021), here we add another layer of external validation (EV), ran on an external dataset. To this goal, we exploited the second release of the AIforCOVID dataset, which contains data collected from 283 patients belonging to other two centers, as already mentioned in section 3.

### 5.6. Performance metrics and statistical assessments

The accuracy, the sensitivity and the specificity are the evaluation metrics used to assess the performance, as in Soda et al. (2021).

Furthermore, we apply the one-way ANOVA among the different groups of models and, to interpret the statistical significance, we used the pairwise Tukey test with a Bonferroni p-value correction at  $\alpha = 0.05$ . Henceforth, we refer to a statistically significant difference when this test is satisfied.

## 6. Results and Discussions

In this section we first show the results of the aforementioned experiments for the classification task, then we verify if the model is interpreting the data in the correct manner via the XAI methods introduced in section 4.

### 6.1. Classification Task

Before presenting the numeric results, let us report that the Pareto optimum  $\Gamma^*$  is composed of three CNNs and one MLP, namely the GoogLeNet, the VGG13-BN, the ResNeXt50-32x4d, and the MLP-2. It is worth noting that the selected models belong to different families suggesting that each extrapolates different information to satisfy the desired classification. Moreover, we understand that the two modalities all give useful and distinct information for the prognosis task, since we have at least one model for each modality. Furthermore, we also ran the multi-objective optimization fusing the learners in each  $\Gamma_I$  applying end-to-end training rather than late fusion to investigate if any differences exist<sup>2</sup>. The results reveal that both provided the same  $\Gamma^*$ , confirming that

---

<sup>2</sup>For computational restrictions during end-to-end training, we limited the number of possible architectures in  $\Gamma_I$  for each modality to a maximum of 3.



Table 1: Performance of all the learners. Note that results marked by an \*, i.e. those of HC, HYB and ETE are extracted from Soda et al. (2021) and do not apply to the external dataset.

	Model	CV			LOCO			EV		
		Acc	TPR	TNR	Acc	TPR	TNR	Acc	TPR	TNR
Proposals	JLF-C-1	79.75±0.23	82.47±0.37	76.81±0.24	77.86±0.33	79.95±0.17	75.95±0.30	77.61±1.10	79.18±1.21	75.38±1.11
	JLF-C-2	79.63±0.24	80.99±0.17	78.90±0.23	77.30±0.32	79.06±0.22	75.88±0.17	76.82±1.22	79.50±1.26	74.23±1.23
	JLF-S-1	79.63±0.16	82.47±0.15	76.67±0.20	77.39±0.29	80.00±0.27	75.52±0.14	77.90±1.27	78.70±1.24	75.96±1.21
	JLF-S-2	79.39±0.17	81.43±0.16	76.69±0.25	77.16±0.30	79.98±0.25	75.89±0.11	76.54±1.25	79.97±1.23	74.73±1.16
Competitors	LF-MV	78.41±0.32	80.09±0.31	76.24±0.22	75.48±0.29	77.98±0.20	73.82±0.21	74.88±1.13	77.64±1.14	73.15±1.11
	LF-P-1	77.38±0.24	79.87±0.22	75.18±0.37	74.65±0.19	76.67±0.30	72.96±0.15	73.85±1.15	76.56±1.22	72.06±1.35
	LF-P-2	77.37±0.29	79.78±0.28	75.11±0.35	74.60±0.16	76.58±0.34	72.88±0.09	73.74±1.15	76.53±1.24	72.00±1.31
	LF-D-1	77.40±0.20	79.95±0.27	75.22±0.30	74.67±0.25	76.60±0.31	72.94±0.03	73.80±1.25	76.55±1.26	72.09±1.22
	LF-D-2	77.34±0.18	79.90±0.29	75.20±0.29	74.58±0.24	76.49±0.27	72.87±0.24	73.71±1.22	76.39±1.23	72.00±1.26
	JF-C	72.80±0.63	76.62±0.83	68.62±0.98	70.35±0.47	71.04±0.52	67.95±0.73	72.47±1.29	78.76±1.44	68.24±1.39
	JF-M	75.00±0.76	78.30±0.71	71.47±0.85	71.37±0.49	74.59±0.65	70.47±0.49	71.64±1.37	75.06±1.41	69.90±1.83
	HC*	75.50±0.70	75.80±0.80	75.30±1.30	75.20±6.70	71.10±16.50	82.40±15.40	-	-	-
	HYB*	76.90±5.40	78.80±6.40	74.70±5.90	74.30±6.10	76.90±18.90	68.50±15.50	-	-	-
	ETE*	74.80±0.80	74.50±1.70	75.10±1.50	70.90±0.50	73.40±1.80	69.60±0.90	-	-	-

performing the optimization in late fusion rather in an end-to-end fashion is a viable alternative that strongly reduces the computation time since the former does not require any additional training.

The quantitative results achieved by all the learners presented in section 5 are shown in Table 1, which shows the average accuracy (Acc), sensitivity (TPR) and specificity (TNR), with the respective standard deviations, for the CV, LOCO, and EV scenarios. The results reveal that the four joint-late methods, i.e. the first four rows in Table 1, outperform the other techniques, and the performance differences against the other multimodal approaches are statistically significant in terms of accuracy, sensitivity and specificity. In particular, these significant differences between JLF and LF-MV, LF-P and LF-D methods demonstrate that the end-to-end training of the method is effective and provide better results than the late fusion of the networks in the ensemble. As mentioned in section 5.4, this result displays *when* the models in the ensemble should be fused.

Let us now focus on the comparison between the four JLF methods and the other two approaches providing an embedded multimodal representation, namely the JF-C, JF-M competitors described in section 2. We find that the JLF performance are statically different in terms of accuracy, sensitivity and

Table 2: Performance single modality models of  $\Gamma^*$  in JLF

Model	Data	CV			LOCO			EV		
		Acc	TPR	TNR	Acc	TPR	TNR	Acc	TPR	TNR
MLP-2	CLI	74.87±1.46	75.95±1.39	72.50±1.76	73.91±1.29	76.37±1.10	70.39±1.37	71.44±2.82	74.17±2.68	68.08±2.98
GoogLeNet	IMG	74.61±0.20	75.99±0.44	72.37±0.65	71.68±0.75	72.58±0.38	70.58±0.94	73.36±1.95	74.73±1.88	71.54±1.37
VGG13-BN	IMG	73.04±0.38	75.67±0.23	70.86±0.47	71.25±0.39	72.28±0.02	70.72±0.20	71.78±1.48	72.98±1.92	70.86±1.29
ResNeXt50	IMG	72.91±0.86	73.90±0.87	71.07±0.38	67.43±0.28	70.08±0.10	65.60±0.10	73.33±1.65	75.73±1.10	70.62±1.28

specificity with respect to those attained by the JF-C, JF-M techniques. This finding points out *how* the individual learners should be combined to provide a useful embedded multimodal representation.

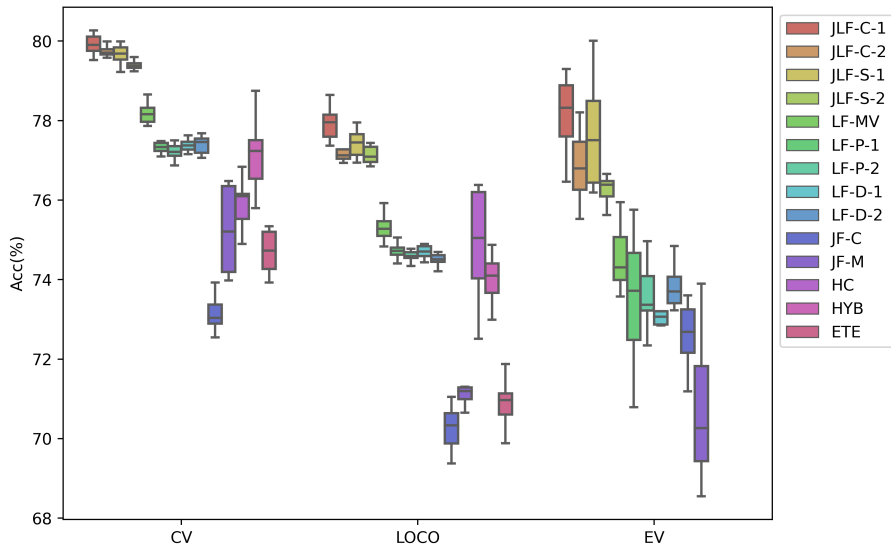
We also found that the performance of JLF models are statistically different when compared with those presented in Soda et al. (2021) (i.e. HC, HYB and ETE), which are the current baseline for the AIforCOVID dataset.

Turning our attention to the comparison between the four set-ups of the JLF approach, the results reveal that no statistically significant differences exist among their performance, suggesting that there is no preferred technique between them, while JFL-C-1 provides the best accuracy in both CV and LOCO experiments.

We are now interested in assessing to what extent our optimization algorithm effectively detects  $\Gamma^*$  as the best choice of *which* learners should be combined among all the possible  $\Gamma_I$ . To this end, we randomly picked 100 different  $\Gamma_I$  that are joint using the JFL-C-1 technique for the reason mentioned a few lines above. Next, we compare these performance against the four JLF results in Table 1 that are achieved using  $\Gamma^*$ , and we find that they are statistically significantly lower.

We now focus on the unimodal scenario to investigate the performance in JLF when a modality is missing: to this end Table 2 shows the results of single models in  $\Gamma^*$  when trained on a single modality. By performing the statistical assessments we find that there is no significant change with the unimodal results presented in Soda et al. (2021), as it could be expected. Note also that for the sake of presentation in Table 2 we do not report all the results attained by all the CNNs and MLPs considered. Nevertheless, GoogLeNet, VGG13-BN and

Figure 3: Distribution of the performance accuracy of all the presented models and competitors in all the training configuration scenarios.



ResNeXt50 are actually the first, the second and the sixth, among the CNNs, respectively, whilst MLP-2 is the first among the other MLPs. Comparing the four JLF learners with these unimodal networks, we find that the former provide performance that are always statistically larger than those returned by the latter, confirming the importance of the fusion between the modalities.

Let us now concentrate on a single modality. Since  $\Gamma^*$  is composed of three CNNs working on the image modality, we perform an ablation test removing the network using clinical data (i.e. MLP-2). In this case, JLF-C-1 achieves an average accuracy equal to  $76.09 \pm 0.29$ ,  $75.68 \pm 0.31$  and  $74.86 \pm 0.27$  in CV, LOCO and EV, respectively. Since these values are statistically lower than those of JLF, we deem that joining multiple networks is beneficial. Furthermore, note that the apposite ablation test, i.e. removing the networks using image data, corresponds to consider MLP-2 only, whose performance are already shown in Table 2.

As a further observation, let us now focus on the different performance

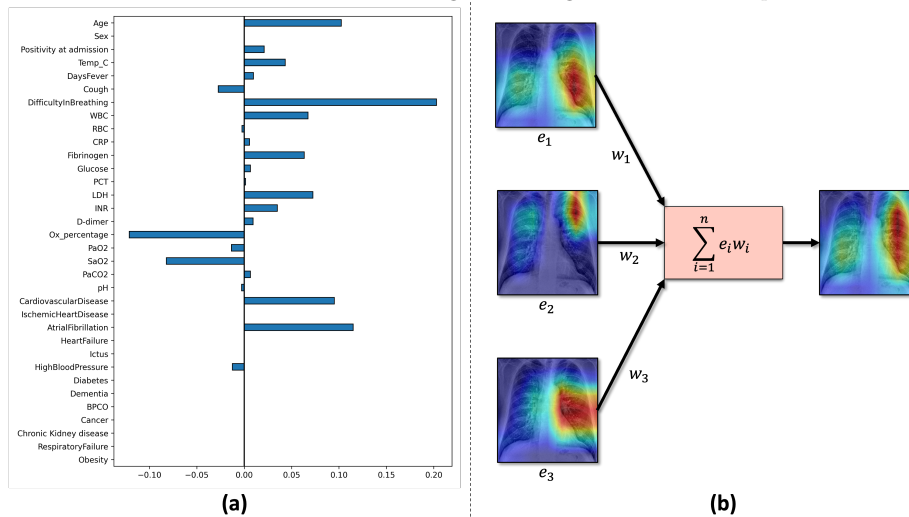
achieved in 10-fold CV, LOCO and EV. To make the comparison easier, Figure 3 shows the distribution of the performance of the different methods across all the experimental scenarios. Observing the results of the JLF methods, we notice that the method is robust and generalizable since the performance drop in LOCO and in EV is limited, while all the others suffer from a larger decrease.

*Explainability.* To open the black-box nature of the multimodal deep approach presented in this work, we apply the XAI algorithms introduced in section 4 to the model with the highest performance, i.e. JLF-C-1.

To this end, we first extract the weights coming out of the classification vector which are connected to the next hidden layer of the FC network; second, we compute the mean relative intensities of such weights attained in CV, obtaining the following distribution: 17%, 26%, 16%, and 41% for GoogLeNet, VGG13-BN, ResNeXt50, and MLP-2, respectively. This information not only makes us understand the importance of every single model for the final classification, but it also explains the hierarchy inter- and intra-modality. In particular, we notice that the image modality has more importance than the clinical one since the relative vector weights are 59% and 41%, respectively. Even if there is a discrepancy between the number of models per modality, it is interesting to notice that MLP-2 has the highest importance among the single neural networks, but the combination of the three CNNs gives higher relative importance to the image modality. Going deeper, we can see that there is also an intra-modality hierarchy between the image-based models, where by calculating the relative weight importances on GoogLeNet, VGG13-BN, and ResNeXt50, we obtain 29%, 44%, and 27%, respectively.

To enable physicians to explore and understand data-driven DL-based systems, we work on XAI algorithms for single models. For each model composing the joint fusion, we apply XAI algorithms suited for the specific modality. For example, Figure 4 shows the results of the integrated gradients algorithm Sundararajan et al. (2017) applied to MLP-2, which shows the importance of the clinical features for the classification. We notice that the most important fea-

Figure 4: XAI modality algorithms: a) feature importance of Integrated Gradients of an instance applied to MLP-2; b) activation maps of Grad-CAM on GoogLeNet, VGG13-BN, and ResNeXt50 which are combined resulting in the weighted activation map



tures are the difficulty in breathing and the oxygen percentage in blood. Indeed, the presence of difficulty in breathing and lower values in the oxygen percentage in the blood are indications of the severe COVID-19 cases as also the medical literature confirms Kermali et al. (2020). Going forward, we can use the aforementioned relative weights of the classification vector for a specific modality to combine the results coming from an XAI algorithm. Still in Figure 4, we show the feature maps extracted from GoogLeNet, VGG13-BN, ResNeXt50 by applying Grad-CAM Selvaraju et al. (2017), and by combining them via equation 12 we obtain a resulting map for the modality. In this way we understand how the different components working on the image modality, and as a whole, interpret the pixel values. Many more XAI algorithms can be applied following this methodology, but to prevent redundancy we limit ourselves to these examples. We did not perform any evaluation on the XAI methods, since it is out of our scope of the presented method.

## 7. Conclusions

In this manuscript we have presented an approach to build an optimized multimodal end-to-end model exploiting a performance metric and the diversity of different neural networks. It addresses open issues in MDL related to *when*, *which* and *how* the modalities and the related learners must be joined to provide effective embedded representation and satisfactory performance. Given the impact of the COVID-19 pandemic, we applied our method to predict patients' prognosis, a topic that has attracted recent research after the large efforts towards the detection of COVID-19 signs in medical images Wynants et al. (2020). In this scenario, the use of different modalities capturing different aspects of the disease progression should be useful and, for this reason, we used the AIforCOVID dataset Soda et al. (2021), which is the only publicly available dataset containing clinical data and CXR scans. Our proposal algorithmically determines *which* deep architectures for each modality should be fused. Furthermore, here we have investigated *how* and *when* the fusion of the modalities should occur: we find that concatenating the classification vectors of each learner, being either soft or crisp labels, is a viable solution. In terms of performance, our method attains state-of-the-art results, not only outperforming the baseline performance reported in Soda et al. (2021) but also being robust to external validation. Moreover, our method fits well with many XAI algorithms, which allow us to figure out a hierarchy among modalities and they can extract the intra-modality importance of the different features by combining the results of various networks.

Future directions are directed towards three main goals. First, we plan to study a method to minimize the computational costs to extend the number of possible architectures per modality in the case of end-to-end training. Second, to investigate the application of this approach to other multimodal datasets. Third, as medical data should come from different institutions, it would also be interesting to explore the deployment of our approach in a federated learning framework.

## Acknowledgments

This work is partially funded by: POR CAMPANIA FESR 2014 - 2020, AP1-OS1.3 project “Protocolli TC del torace a bassissima dose e tecniche di intelligenza artificiale per la diagnosi precoce e quantificazione della malattia da COVID-19” CUP D54I20001410002; EU project “University-Industrial Educational Centre in Advanced Biomedical and Medical Informatics (CeBMI) No. 612462-EPP-1-2019-1-SK-EPPKA2-KA”. The authors would like to thank the team collecting and making publicly available the AIforCOVID dataset.

## References

- Al-Najjar, H., Al-Rousan, N., 2020. A classifier prediction model to predict the status of Coronavirus COVID-19 patients in South Korea. *European Review for Medical and Pharmacological Sciences* .
- Arcuri, A., Fraser, G., 2013. Parameter tuning or default values? An empirical investigation in search-based software engineering. *Empirical Software Engineering* 18, 594–623.
- Arrieta, A.B., Díaz-Rodríguez, N., Del Ser, J., Bennetot, A., Tabik, S., Barbado, A., García, S., Gil-López, S., Molina, D., Benjamins, R., et al., 2020. Explainable artificial intelligence (XAI): Concepts, taxonomies, opportunities and challenges toward responsible AI. *Information Fusion* 58, 82–115.
- Bai, X., Fang, C., Zhou, Y., Bai, S., Liu, Z., Xia, L., Chen, Q., Xu, Y., Xia, T., Gong, S., et al., 2020. Predicting COVID-19 malignant progression with AI techniques .
- Baltrušaitis, T., Ahuja, C., Morency, L.P., 2018. Multimodal machine learning: A survey and taxonomy. *IEEE transactions on pattern analysis and machine intelligence* 41, 423–443.

- Bengio, Y., Courville, A., Vincent, P., 2013. Representation learning: A review and new perspectives. *IEEE Transactions on Pattern Analysis and Machine Intelligence* 35, 1798–1828.
- Chamola, V., Hassija, V., Gupta, V., Guizani, M., 2020. A comprehensive review of the COVID-19 pandemic and the role of IoT, drones, AI, blockchain, and 5G in managing its impact. *IEEE Access* 8, 90225–90265.
- Chen, R.J., Lu, M.Y., Wang, J., Williamson, D.F., Rodig, S.J., Lindeman, N.I., Mahmood, F., 2020. Pathomic fusion: an integrated framework for fusing histopathology and genomic features for cancer diagnosis and prognosis. *IEEE Transactions on Medical Imaging* .
- Cohen, J.P., Morrison, P., Dao, L., Roth, K., Duong, T.Q., Ghassemi, M., 2020. COVID-19 image data collection: Prospective predictions are the future. *arXiv preprint arXiv:2006.11988* .
- Deng, J., Dong, W., Socher, R., Li, L.J., Li, K., Fei-Fei, L., 2009. ImageNet: A large-scale hierarchical image database, in: *2009 IEEE Conference on Computer Vision and Pattern Recognition*, IEEE. pp. 248–255.
- Fang, C., Bai, S., Chen, Q., Zhou, Y., Xia, L., Qin, L., Gong, S., Xie, X., Zhou, C., Tu, D., et al., 2021. Deep learning for predicting covid-19 malignant progression. *Medical Image Analysis* 72, 102096.
- Glorot, X., Bengio, Y., 2010. Understanding the difficulty of training deep feedforward neural networks, in: *Proceedings of the Thirteenth International Conference on Artificial Intelligence and Statistics, JMLR Workshop and Conference Proceedings*. pp. 249–256.
- Glorot, X., Bordes, A., Bengio, Y., 2011. Deep sparse rectifier neural networks, in: *Proceedings of the Fourteenth International Conference on Artificial Intelligence and Statistics, JMLR Workshop and Conference Proceedings*. pp. 315–323.



- Guarrasi, V., D'Amico, N.C., Sicilia, R., Cordelli, E., Soda, P., 2021. A multi-expert system to detect covid-19 cases in x-ray images, in: 2021 IEEE 34th International Symposium on Computer-Based Medical Systems (CBMS), IEEE. pp. 395–400.
- Guarrasi, V., D'Amico, N.C., Sicilia, R., Cordelli, E., Soda, P., 2022. Pareto optimization of deep networks for COVID-19 diagnosis from chest X-rays. *Pattern Recognition* 121, 108242.
- He, K., Zhang, X., Ren, S., Sun, J., 2016. Deep residual learning for image recognition, in: *Proceedings of the IEEE Conference on Computer Vision and Pattern Recognition*, pp. 770–778.
- Hendricks, L.A., Burns, K., Saenko, K., Darrell, T., Rohrbach, A., 2018. Women also snowboard: Overcoming bias in captioning models, in: *Proceedings of the European Conference on Computer Vision (ECCV)*, pp. 771–787.
- Huang, G., Liu, Z., Van Der Maaten, L., Weinberger, K.Q., 2017. Densely connected convolutional networks, in: *Proceedings of the IEEE Conference on Computer Vision and Pattern Recognition*, pp. 4700–4708.
- Jaeger, S., Candemir, S., Antani, S., Wang, Y.X.J., Lu, P.X., Thoma, G., 2014. Two public chest X-ray datasets for computer-aided screening of pulmonary diseases. *Quantitative Imaging in Medicine and Surgery* 4, 475.
- John, F., 2014. Extremum problems with inequalities as subsidiary conditions, in: *Traces and Emergence of Nonlinear Programming*. Springer, pp. 197–215.
- Joshi, G., Walambe, R., Kotecha, K., 2021. A review on explainability in multimodal deep neural nets. *IEEE Access* .
- Joze, H.R.V., Shaban, A., Iuzzolino, M.L., Koishida, K., 2020. MMTM: Multimodal transfer module for CNN fusion, in: *Proceedings of the IEEE/CVF Conference on Computer Vision and Pattern Recognition*, pp. 13289–13299.

- Karpathy, A., Toderici, G., Shetty, S., Leung, T., Sukthankar, R., Fei-Fei, L., 2014. Large-scale video classification with convolutional neural networks, in: Proceedings of the IEEE Conference on Computer Vision and Pattern Recognition, pp. 1725–1732.
- Kermali, M., Khalsa, R.K., Pillai, K., Ismail, Z., Harky, A., 2020. The role of biomarkers in diagnosis of COVID-19: A systematic review. *Life Sciences* 254, 117788.
- Kim, H.J., Frahm, J.M., 2018. Hierarchy of alternating specialists for scene recognition, in: Proceedings of the European Conference on Computer Vision (ECCV), pp. 451–467.
- Krizhevsky, A., 2014. One weird trick for parallelizing convolutional neural networks. arXiv preprint arXiv:1404.5997 .
- Kuhn, H.W., Tucker, A.W., 2014. Nonlinear programming, in: *Traces and Emergence of Nonlinear Programming*. Springer, pp. 247–258.
- Kumar, V., Minz, S., 2014. Feature selection: a literature review. *SmartCR* 4, 211–229.
- Kuncheva, L.I., Whitaker, C.J., 2003. Measures of diversity in classifier ensembles and their relationship with the ensemble accuracy. *Machine Learning* 51, 181–207.
- Ma, N., Zhang, X., Zheng, H.T., Sun, J., 2018. ShuffleNet V2: Practical guidelines for efficient CNN architecture design, in: Proceedings of the European Conference on Computer Vision (ECCV), pp. 116–131.
- Montavon, G., Lapuschkin, S., Binder, A., Samek, W., Müller, K.R., 2017. Explaining nonlinear classification decisions with deep Taylor decomposition. *Pattern Recognition* 65, 211–222.
- Neverova, N., Wolf, C., Taylor, G., Nebout, F., 2015. ModDrop: adaptive multi-modal gesture recognition. *IEEE Transactions on Pattern Analysis and Machine Intelligence* 38, 1692–1706.

- Ngiam, J., Khosla, A., Kim, M., Nam, J., Lee, H., Ng, A.Y., 2011. Multimodal deep learning, in: International Conference on Machine Learning.
- Ning, W., Lei, S., Yang, J., Cao, Y., Jiang, P., Yang, Q., Zhang, J., Wang, X., Chen, F., Geng, Z., et al., 2020. Open resource of clinical data from patients with pneumonia for the prediction of COVID-19 outcomes via deep learning. *Nature Biomedical Engineering* 4, 1197–1207.
- Nojavanasghari, B., Gopinath, D., Koushik, J., Baltrušaitis, T., Morency, L.P., 2016. Deep multimodal fusion for persuasiveness prediction, in: Proceedings of the 18th ACM International Conference on Multimodal Interaction, pp. 284–288.
- Ozsahin, I., Sekeroglu, B., Musa, M.S., Mustapha, M.T., Uzun Ozsahin, D., 2020. Review on diagnosis of COVID-19 from chest CT images using artificial intelligence. *Computational and Mathematical Methods in Medicine* 2020.
- Rajaraman, S., Siegelman, J., Alderson, P.O., Folio, L.S., Folio, L.R., Antani, S.K., 2020. Iteratively pruned deep learning ensembles for COVID-19 detection in chest X-rays. *IEEE Access* 8, 115041–115050.
- Ramachandram, D., Lisicki, M., Shields, T.J., Amer, M.R., Taylor, G.W., 2018. Bayesian optimization on graph-structured search spaces: Optimizing deep multimodal fusion architectures. *Neurocomputing* 298, 80–89.
- Ramachandram, D., Taylor, G.W., 2017. Deep multimodal learning: A survey on recent advances and trends. *IEEE Signal Processing Magazine* 34, 96–108.
- Ronneberger, O., Fischer, P., Brox, T., 2015. U-Net: Convolutional networks for biomedical image segmentation, in: International Conference on Medical Image Computing and Computer-Assisted Intervention, Springer. pp. 234–241.
- Sandler, M., Howard, A., Zhu, M., Zhmoginov, A., Chen, L.C., 2018. MobileNetV2: Inverted residuals and linear bottlenecks, in: Proceedings of the

- IEEE Conference on Computer Vision and Pattern Recognition, pp. 4510–4520.
- Selvaraju, R.R., Cogswell, M., Das, A., Vedantam, R., Parikh, D., Batra, D., 2017. GRAD-CAM: Visual explanations from deep networks via gradient-based localization, in: Proceedings of the IEEE International Conference on Computer Vision, pp. 618–626.
- Shiraishi, J., Katsuragawa, S., Ikezoe, J., Matsumoto, T., Kobayashi, T., Komatsu, K.i., Matsui, M., Fujita, H., Kodera, Y., Doi, K., 2000. Development of a digital image database for chest radiographs with and without a lung nodule: receiver operating characteristic analysis of radiologists’ detection of pulmonary nodules. *American Journal of Roentgenology* 174, 71–74.
- Shrikumar, A., Greenside, P., Kundaje, A., 2017. Learning important features through propagating activation differences, in: International Conference on Machine Learning, PMLR. pp. 3145–3153.
- Signoroni, A., Savardi, M., Benini, S., Adami, N., Leonardi, R., Gibellini, P., Vaccher, F., Ravanelli, M., Borghesi, A., Maroldi, R., et al., 2021. BS-Net: Learning COVID-19 pneumonia severity on a large chest X-ray dataset. *Medical Image Analysis* 71, 102046.
- Simonyan, K., Zisserman, A., 2014. Very deep convolutional networks for large-scale image recognition. *arXiv preprint arXiv:1409.1556* .
- Soda, P., D’Amico, N.C., Tessadori, J., Valbusa, G., Guarrasi, V., Bortolotto, C., Akbar, M.U., Sicilia, R., Cordelli, E., Fazzini, D., et al., 2021. AIfor-COVID: predicting the clinical outcomes in patients with COVID-19 applying AI to chest-X-rays: an italian multicentre study. *Medical Image Analysis* 74, 102216.
- Stahlschmidt, S.R., Ulfenborg, B., Synnergren, J., 2022. Multimodal deep learning for biomedical data fusion: a review. *Briefings in Bioinformatics* .

- Sundararajan, M., Taly, A., Yan, Q., 2017. Axiomatic attribution for deep networks, in: International Conference on Machine Learning, PMLR. pp. 3319–3328.
- Szegedy, C., Liu, W., Jia, Y., Sermanet, P., Reed, S., Anguelov, D., Erhan, D., Vanhoucke, V., Rabinovich, A., 2015. Going deeper with convolutions, in: Proceedings of the IEEE Conference on Computer Vision and Pattern Recognition, pp. 1–9.
- Tan, M., Chen, B., Pang, R., Vasudevan, V., Sandler, M., Howard, A., Le, Q.V., 2019. MnasNet: Platform-aware neural architecture search for mobile, in: Proceedings of the IEEE/CVF Conference on Computer Vision and Pattern Recognition, pp. 2820–2828.
- Wu, Y., Arribas, J.I., 2003. Fusing output information in neural networks: Ensemble performs better, in: Proceedings of the 25th Annual International Conference of the IEEE Engineering in Medicine and Biology Society, IEEE. pp. 2265–2268.
- Wynants, L., Van Calster, B., Collins, G.S., Riley, R.D., Heinze, G., Schuit, E., Bonten, M.M., Dahly, D.L., Damen, J.A., Debray, T.P., et al., 2020. Prediction models for diagnosis and prognosis of COVID-19: systematic review and critical appraisal. *BMJ* 369.
- Zadeh, A., Chen, M., Poria, S., Cambria, E., Morency, L.P., 2017. Tensor fusion network for multimodal sentiment analysis. *arXiv preprint arXiv:1707.07250*.
- Zhu, J.S., Ge, P., Jiang, C., Zhang, Y., Li, X., Zhao, Z., Zhang, L., Duong, T.Q., 2020. Deep-learning artificial intelligence analysis of clinical variables predicts mortality in COVID-19 patients. *Journal of the American College of Emergency Physicians Open* 1, 1364–1373.

## Appendix A. Clinical data

Table A.1: Description of the clinical data coming from Soda et al. (2021). Feature names followed by + were not used.

Name	Description
Active cancer in the last 5 years	Patient had active cancer in the last 5 years
Age	Patient's age (years)
Atrial Fibrillation	Patient had atrial fibrillation
Body temperature ( $^{\circ}\text{C}$ )	Patients temperature at admission (in $^{\circ}\text{C}$ )
Cardiovascular Disease	Patient had cardiovascular diseases
Chronic Kidney disease	Patient had chronic kidney disease
COPD	Chronic obstructive pulmonary disease
Cough	Cough presence
CRP	C-reactive protein concentration (mg/dL)
Days Fever	Days of fever up to admission (days)
D-dimer	D-dimer amount in blood
Death+	Death of patient occurred during hospitalization for any cause
Dementia	Patient had dementia
Diabetes	Patient had diabetes
Dyspnea	Patient had intense tightening in the chest, air hunger, difficulty breathing, breathlessness or a feeling of suffocation
Fibrinogen	Fibrinogen concentration in blood (mg/dL)
Glucose	Glucose concentration in blood (mg/dL)
Heart Failure	Patient had heart failure
Hypertension	Patient had high blood pressure
INR	International Normalized Ratio
Ischemic Heart Disease	Patient had ischemic heart disease
LDH	Lactate dehydrogenase concentration in blood (U/L)
$\text{O}_2$ (%)	Oxygen percentage in blood (%)
Obesity	Patient had obesity
$\text{PaCO}_2$	Partial pressure of carbon dioxide in arterial blood (mmHg)
$\text{PaO}_2$	Partial pressure of oxygen in arterial blood (mmHg)
PCT	Platelet count (ng/mL)
pH	Blood pH
Position+	Patient position during chest x-ray (%supine)
Positivity at admission	Positivity to the SARS-CoV-2 swab at the admission time
Prognosis	Patient outcome
RBC	Red blood cells count ( $10^9/\text{L}$ )
Respiratory Failure	Patient had respiratory failure
$\text{SaO}_2$	Arterial oxygen saturation (%)
Sex	Patient's sex
Stroke	Patient had stroke
Therapy Anakinra+	Patient was treated with Anakinra
Therapy anti-inflammatory+	Patient was treated with anti-inflammatory drugs therapy
Therapy antiviral+	Patient was treated with antiviral drugs
Therapy Eparine+	Patient was treated with eparine treatment; therapeutic treatment
Therapy hydroxychloroquine+	Patient was treated with hydroxychloroquine
Therapy Tocilizumab+	Patient was treated with Tocilizumab
WBC	White blood cells count ( $10^9/\text{L}$ )